

Dynamical triggering of tremors near Nanao, Taiwan, by the 2011 Tohoku earthquake: Slab-related fluid-induced seismicity

Yi-Hsuan Wu¹, Wu-Cheng Chi², Liam Chai³, and Chin-Jen Lin⁴

¹Institute of Earth Sciences, Academia Sinica

²Academia Sinica

³University of Chicago

⁴Institute of Earth Sciences, Academia Sinica, Taiwan

November 28, 2022

Abstract

Dynamic triggering has been documented in many places in both seismic active and inactive regions, and most triggered events are tremors. These tremors provide a scaling relationship that bridges natural earthquakes and laboratory experiments. In particular, dynamic triggering may help understand the rupture mechanism of natural earthquakes. The Nanao array, a small aperture array composed of 4 dual broadband and strong motion seismic stations in Taiwan, recorded the 2011 Tohoku M9 earthquake and locally triggered tremors, in addition to the ambient tremors. Using Spudich's method to derive shallow crustal shear strain, dilation, and rotation during tremor episodes, we found that tremors occurred when dilation was larger than 10^{-8} , similar to Nankai Trough cases. Previous tomographic studies have shown partial melting coming from the dehydration of the subducting Ryukyu slab and the slab edge corner. Such a partial melt zone extends to shallow depth near the Nanao array and could potentially elevate the pore fluid temperature. A systematic check of all the seismic stations in Northern Taiwan shows clear increased triggered tremors only near Nanao right after the Tohoku earthquake. We applied array processing methods to the Nanao array data and derived a NE to SW back azimuth directions of the tremors, filling a seismic gap in northeastern Taiwan seismicity six months after Tohoku earthquake. Analogous to fluid-related acoustic emission lab experiments, we propose that this is among the first field examples of dynamically triggered tremors associated with moving fluids from a slab and its edge.

Hosted file

dynamicaltriggeringsi_jgr_resubmission2.docx available at <https://authorea.com/users/554375/articles/606848-dynamical-triggering-of-tremors-near-nanao-taiwan-by-the-2011-tohoku-earthquake-slab-related-fluid-induced-seismicity>

**Dynamical triggering of tremors near Nanao, Taiwan, by the 2011
Tohoku earthquake: Slab-related fluid-induced seismicity**

Yi-Hsuan Wu^{1*}, Wu-Cheng Chi¹, Liam Chai², and Chin-Jen Lin¹

¹Institute of Earth Sciences, Academia Sinica, Taipei, Taiwan

²Taipei American School, Taipei, Taiwan

Corresponding author: Yi-Hsuan Wu (maomao@earth.sinica.edu.tw)

Key Points:

- The wave train of Tohoku earthquake dynamically triggered shallow tremors above the edge of a subducted slab.
- Waveforms from a small aperture array allowed the derivation of dynamic crustal shear strains and dilations when tremors were triggered.
- The triggering mechanism of tremors is analogous to decompression and fluid-rock interaction in fluid-induced seismicity lab experiments.

1 **Abstract**

2 Dynamic triggering has been documented in many places in both seismic active and
3 inactive regions, and most triggered events are tremors. These tremors provide a scaling
4 relationship that bridges natural earthquakes and laboratory experiments. In particular,
5 dynamic triggering may help understand the rupture mechanism of natural earthquakes.
6 The Nanao array, a small aperture array composed of 4 dual broadband and strong motion
7 seismic stations in Taiwan, recorded the 2011 Tohoku M9 earthquake and locally
8 triggered tremors, in addition to the ambient tremors. Using Spudich's method to derive
9 shallow crustal shear strain, dilation, and rotation during tremor episodes, we found that
10 tremors occurred when dilation was larger than 10^{-8} , similar to Nankai Trough cases.
11 Previous tomographic studies have shown partial melting coming from the dehydration of
12 the subducting Ryukyu slab and the slab edge corner. Such a partial melt zone extends to
13 shallow depth near the Nanao array and could potentially elevate the pore fluid
14 temperature. A systematic check of all the seismic stations in Northern Taiwan shows
15 clear increased triggered tremors only near Nanao right after the Tohoku earthquake. We
16 applied array processing methods to the Nanao array data and derived a NE to SW back
17 azimuth directions of the tremors, filling a seismic gap in northeastern Taiwan seismicity
18 six months after Tohoku earthquake. Analogous to fluid-related acoustic emission lab
19 experiments, we propose that this is among the first field examples of dynamically
20 triggered tremors associated with moving fluids from a slab and its edge.

21

22 **Plain Language Summary**

23 Unlike earthquakes, tremors generate signals with gentle beginning and throughout to the
24 end. The origin of non-volcanic tremors is still not clear, but has been linked to different
25 ways the crust slips on a fault with the help of fluids. Thus, such tremors might help us to
26 understand the physics of earthquake. We report a new group of tremors in Northern
27 Taiwan in a very localized zone where the edge of a piece of crust goes underneath
28 another crust. Such tremors are unique, rich in high frequency (> 10 Hz). They occurred
29 normally near the shallow crustal edge at Nanao, Taiwan. But additional tremors were
30 triggered by passing waves from other earthquakes. At Nanao, we installed seismometers
31 at 4 sites that were within 500 meters of each other, and recorded the triggered tremors
32 from the M 9.0 Tohoku Earthquake. Due to this dense seismic array, we discovered more
33 triggered tremors in the first part of the passive waves when the crust experienced
34 volumetric changes, instead of the later part when the crust experienced maximum
35 shearing. Such results challenge previous seismic findings but are consistent with
36 recently reported lab experiments.

37 **1 Introduction**

38 Dynamic triggering of seismic events is an active research topic that has implications for
39 earthquake physics and even seismic hazard mitigation. Despite the growing amount of
40 research on dynamic triggering, many questions on the topic still remain. Jiang et al.
41 (2010) identified two main questions regarding the dynamic triggering of earthquakes:
42 What are the necessary geological and other conditions to trigger earthquakes remotely?
43 and What are the physical processes responsible for triggering seismicity at teleseismic
44 distances? Dynamic triggering can occur when teleseismic surface waves pass through.
45 Recently, Velasco et al. (2008) demonstrated that out of 15 Mw7.0+ earthquakes, 12
46 resulted in significant increases in the detection of smaller earthquakes over 500 globally
47 distributed broadband seismograms. Observational studies of dynamic triggering of
48 earthquakes and tremors may greatly improve our understanding of the causative stresses
49 and environmental factors behind long-distance triggering mechanisms.

50

51 Dynamic triggering can favorably occur in geothermal/volcanic regions associated with
52 extensional and transtensional environments (Hill & Prejean, 2007), and in areas with
53 higher background seismicity such as active plate boundaries, as they may be closer to
54 failure (Hill et al., 1993; Hough et al., 2003). Recent studies show that dynamic triggering
55 may also occur in more stable regions with low background seismicity (Gomberg et al.,
56 2004; Velasco et al., 2008). All of these areas are assumed to be critically stressed, so
57 small stress perturbations can trigger events. Whether dynamic triggering can occur in
58 other geological settings is still not clear.

59

60 Many models of the physical processes responsible for dynamic triggering have been
61 proposed and can be generalized to two main categories as summarized by Hill and
62 Prejean (2007). One is triggering by Coulomb failure via different frictional laws
63 (Gomberg et al., 1998, 2005; Gomberg, 2001; Perfettini et al., 2003; Gomberg & Johnson,
64 2005; Johnson & Jia, 2005; Hill, 2008), and the other is dynamic triggering through the
65 excitation of crustal fluids (Linde et al., 1994; Brodsky et al., 1998, 2003; Hill et al.,
66 2002). The tremors are mostly interpreted to be related to fluids.

67

68 Taiwan is a seismic active region due to the collision between Eurasian Plate and
69 Philippine Sea Plate. Thus, it provides a platform for examining tremors and studying the
70 mechanism of dynamic triggering. Chao et al. (2012) studied triggered tremors beneath
71 the Central Range for 45 teleseismic earthquakes and found that 5 of them triggered
72 tremors in the north Central Range. However, the locations of the five tremors have large
73 uncertainties due to a lack of sufficiently dense seismic recordings. The Nanao array,
74 with 5 stations within a 2 km by 2 km footprint and another distant station 24 km away as
75 a reference station, is located at the intersection of multiple plate boundaries, providing
76 an opportunity to observe tremor activity in a region of flipped subduction polarities. In
77 addition, the Nanao array, with its close station spacing, allows us to detect with more
78 confidence the dynamically triggered low amplitude earthquakes that are typically
79 masked by large amplitude earthquakes. The array also allows array processing to
80 characterize the dynamic crustal deformation during teleseismic wave trains, and their
81 relation to the first-order source parameters of the tremors, in case no direct strain meter
82 and ground rotation measurements are available.

83

84 We investigated three sets of one-hour seismic waveforms from the Nanao array before,
85 right after, and after the 2011 Tohoku M9 earthquake with an epicentral distance of
86 around 2485 km, and visually identified ten dynamically triggered tremors. We found and
87 analyzed the characteristics of the ambient tremors, in addition to the proposed triggered
88 tremors. We then determined the dynamic crustal shear strain, dilation, and rotations
89 caused by the teleseismic waves using an inversion technique developed by Spudich
90 (1995) and Spudich and Fletcher (2008, 2009) that has been tested using different codes
91 (e.g. Huang, 2003; Suryanto et al., 2006; and Chi et al., 2011) to learn more about how
92 the tremors were dynamically triggered. A strong correlation between the maximum
93 shear strain and dilation has led us to interpret that the triggered tremors can be associated
94 with crustal fluid processes, as shown in some previous studies (e.g. Dreger et al., 2000;
95 Foulger et al., 2004; Miyazawa & Mori, 2006) and lab experiments. Based on the crustal
96 velocity models and the interpreted melt and fluids along the edge of the subducting
97 Philippine Sea Plate (Lin et al., 2004), we propose that the subducting slab and the slab
98 edge beneath the Nanao array are experiencing dehydration and provide fluids and heat
99 from depth, thus generating a newly discovered class of high frequency ambient tremors,
100 in addition to dynamically triggered shallow tremors, at this particular location; and
101 therefore, such a geological setting can also generate fluid-induced seismicity.

102

103 **2 Nanao Array and The High Frequency Nonvolcanic Tremor (HFNT)**

104 The Nanao array is a semi-permanent seismic array installed by the Institute of Earth
105 Sciences (IES), Academia Sinica, using instruments provided by IES and the Taiwan

106 Earthquake Center (TEC) of Taiwan. This array, situated in Nanao Township of Yilan
107 County, Taiwan, is designed to have three arms with concentric circles to allow special
108 array processing procedures to be applied to the data more easily. It follows the
109 successful Strong-Motion Accelerograph Array in Taiwan, phase 1 and phase 2
110 (SMART-1 and SMART-2) array projects (Chiu et al., 1994; Shin et al., 2003). However,
111 instead of strong motion sensors used in SMART-1 and SMART-2 projects, the Nanao
112 array is composed of Nanometrics Trillium Compact broadband seismometers,
113 Kinematics EpiSensor strong motion sensors, and Eentec R1 rotational sensors.
114 Quanterra Q330 dataloggers were used for data acquisition with a sample rate of 200 Hz.
115 The sensors are located about 2 meters below the surface in a vault-type station to reduce
116 background noise. The waveforms are continuously synchronized to the GPS timing
117 system. This array was partially operational in March 2011. The stations available during
118 the Tohoku earthquake were NA01, NA04, NA05, NA06, NA07, and NAO05 (see Fig. 1).

119

120 The Nanao array is located just to the north of the Coastal Range, an accreted arc to the
121 passive margin, and at the western end of the Ryukyu arc, where uplift of Taiwan is
122 waning as a result of subduction polarity flip (e.g. Teng, 1996; Huang et al., 2012; Van
123 Avendonk et al., 2016). It is located near the juncture of two convergent boundaries. To
124 the south, the Eurasian Plate is subducting to the east underneath the Philippine Sea Plate.
125 To the east of the Nanao array, the Philippine Sea Plate is subducting northward
126 underneath the Eurasian Plate. The rollback of northward subduction resulted in both the
127 opening of Okinawa Trough and Yilan Plain. The interaction between plates induced a
128 large amount of local seismicity and surface deformation. Continuous recordings from

129 the Nanao array provide an opportunity to detect low amplitude ground motions that are
130 typically masked by large earthquakes, potentially leading to a better understanding of
131 small earthquake and tremor triggering mechanisms.

132

133 We studied the velocity seismograms using HHZ channel of Nanao array and compare
134 their waveforms with those of Broadband Array in Taiwan for Seismology (BATS) to
135 examine the seismic characteristics (Fig. 2 and S1-S7). We found tremors with two bands
136 of frequencies, one between 2-8 Hz, while the other > 10 Hz, as observed from their
137 continuous wavelet transform (CWT) (Fig. 2b). The 2-8 Hz signals are typical for
138 nonvolcanic tremors, as documented in many previous studies. However, tremor signals
139 with frequency > 10 Hz are rare. For this work, we call the tremor with 2-8 Hz signals
140 the typical tremor while the tremors with both 2-8 Hz and > 10 Hz signals the High
141 Frequency Nonvolcanic Tremor (HFNT). Both the typical and the high frequency signals
142 show the characteristics of nonvolcanic tremor: none impulsive onset and minutes-long
143 duration recorded across the array without clear P and S phase (Obara, 2002; Beroza and
144 Ide, 2011; Obara and Kato, 2016). Note that some of the 2-8 Hz frequency signals might
145 be noises generated by wind. However, such noises usually have durations of hours (e.g.
146 Johnson et al., 2019), instead of a few minutes we have observed. Some of the 5-20 Hz
147 signals might due to wind interaction with the vegetation (e.g. Johnson et al., 2019) but
148 such noises do not show two clear bands of 2-8 Hz and > 10 Hz. Also, their durations are
149 also hours, not minutes. Some T phases also have 2-8 Hz tremor-like signals (Buehler
150 and Shearer, 2015), but we have not found associated P and S phases before the observed

151 2-8 Hz signals. Thus, we assume that the observed signals are mostly nonvolcanic
152 tremors.

153

154 We also compare the tremors characteristics before, during, and after the Tohoku
155 teleseismic waveforms have passed through Taiwan, particularly Nanao. Three time
156 windows, each with one hour duration, were studied in Fig. 2 for the pre-seismic, co-
157 seismic, and post-seismic periods. Fig. 2(a) and (b) show a relatively quiet period before
158 the Tohoku earthquake (2011-03-10 12:10:00–13:10:00) during which there was no
159 teleseismic but only two local earthquakes (in the last 350 seconds of the time window).
160 Following a very-low-frequency (VLF) event at about 2500 seconds, a significant tremor
161 occurred at about 2600 seconds. This tremor had large amplitude not only at 2-8 Hz
162 frequency band but also at >10 Hz frequency band. Furthermore, the CWT (Fig. 2b)
163 showed that the tremor had two or even three dominant high frequency bands at the same
164 time. Most of the HFNT in the pre-seismic period are related to the VLF events (Fig. 2a,
165 b and S1-S3), these VLF events have small magnitudes based on visual inspection. All
166 the tremors during this time period are considered as ambient tremors, except the ones
167 associated with the VLF events that are out of scope for this study.

168

169 The one-hour seismic waveforms including the Tohoku teleseismic waveforms show
170 similar tremor characteristics. But many of them are assigned as triggered tremors due to
171 the following reasons: They occurred at the same time with the larger teleseismic phases;
172 and the number of the tremors within this hour have increased compared with the pre-
173 and post-seismic periods. The triggered tremors are most active when teleseismic P wave,

174 instead of the surface, arrived (Fig. 2c and 2d), as shown in the high frequency band. We
175 picked another one-hour window long after the Tohoku teleseismic waves (4:30 to 5:30
176 am on March 12). Such post-seismic time window is also considered as a quiet period,
177 with many seismic waveform characteristics (Fig. 2e and 2f) similar to that in the pre-
178 seismic time period. Next, we will mainly focus on using arrayed seismic waveforms to
179 study the triggered tremors when the teleseismic waves passing through Nanao array and
180 Northern Taiwan.

181

182 **3 Array Data Analyses**

183 When the Tohoku earthquake (Mw9.1) occurred on March 11, 2011 at 05:46:23 (UTC),
184 the Nanao array network was under maintenance, thus not all the stations were
185 operational. Fortunately, six stations in the Nanao array equipped with accelerometers
186 recorded the strong motion waveforms of this event and three of the stations also
187 recorded broadband waveforms. Those available stations and their locations are listed in
188 Table S1. The stations with broadband data are labeled by stars. The Japan
189 Meteorological Agency (JMA) places the epicenter of the 2011 Tohoku-oki earthquake at
190 130 km off the Pacific coast of the Tohoku region at 38°06.2'N and 142°51.6'E and at a
191 depth of 24 km. The Nanao array is approximately 2485 km away from the earthquake
192 epicenter. The locations of the epicenter and the Nanao array are shown in Fig. 1.

193

194 In order to investigate all the events triggered by the main shock wave trains, we chose a
195 one-hour time window starting from the origin time of main shock. We analyzed each
196 vertical component seismic waveform in channels HHZ and HLZ, which represent

197 broadband and strong motion, respectively. The displacement waveforms derived from
198 double-time integration of the accelerometers show a high similarity with displacement
199 derived from the broadband seismometers. We compare the time series data within our
200 study period and obtain high correlation coefficients of 0.9995, 0.9980, and 0.9984 for
201 stations NA04, NA06, and NA07, respectively. Because the strain inversion method
202 needs at least 3 stations, we performed the analysis and calculations on waveforms from
203 accelerometers in this study.

204

205 To detect the triggered events hidden in high amplitude arrivals from the main shock, we
206 applied a 5 Hz high pass filter to the waveforms recorded by the Nanao array following
207 Gonzalez-Huizar and Velasco (2011), and Peng and Chao (2008). One main reason for
208 choosing 5 Hz high pass filter instead of using 1-10 Hz or 2-8 Hz bandpass filter is that
209 mainshock waveforms have unusually strong P and S coda with signals up to 5 Hz. In
210 addition, the tremor signals in Nanao inherently have high frequency component. After
211 applying the high pass filter to the waveforms, we visually inspected the seismogram and
212 identified events with characteristics of dynamically triggered tremors reported in
213 previous studies (Chao et al., 2013; Jiang et al., 2010; Sun et al., 2015; Velasco et al.,
214 2008).

215

216 We picked tremor durations using visual inspection of the seismograms and auto-
217 detection from the spectrograms. Comparing the spectrograms with the seismograms, we
218 found that tremors recorded across the stations have coherent signals up to 15 Hz and the
219 signals scattered when the frequency is higher than 20 Hz. Thus, we designed an auto-

220 detection process, that is to calculate the mean energy and the standard deviation of
221 energy at 15 Hz for the whole study period, then picked the signals with energy beyond
222 two standard deviations at that frequency. Furthermore, we compared waveforms in
223 different stations during the time span of potential tremors obtained from a spectrogram
224 auto-detection method and adjusted the time span to pick the time window, and make
225 sure the onset time of triggered tremors in different stations would be included.

226

227 Finally, we inverted the local maximum shear strain, dilation, and rotation when the
228 tremors were triggered, and inspected their spatiotemporal variation using different
229 station configurations and different time windows. We used a software developed by
230 Spudich et al. (1995) and Spudich and Fletcher (2008, 2009) to infer the shear strain
231 tensor, rigid body rotation tensor, and the angle of rotation caused by the seismic wave.
232 This method is reliable for deriving vertical rotational synthetics using horizontal
233 waveforms from array observations (e.g. Huang, 2003; Suryanto et al., 2006; Chi et al.,
234 2011; and Donner et al., 2017). Appendix A of Spudich et al. (1995) and the text of
235 Spudich and Fletcher (2009) have elegantly documented their derivation. The formulation
236 implemented in the software of Spudich et al. (1995) and Spudich and Fletcher (2008,
237 2009) assumes that the displacement gradient tensor was spatially uniform beneath the
238 array. As a result, seismic signals with wavelength l shorter than $4h$, where h is the
239 horizontal extent of the array, have to be filtered out. Combining with the relation that
240 $l = c/f$, where c is phase velocity and f is frequency, the maximum usable frequency is
241 $f_{\max} = c/4h$. In order to obtain reliable inversion, we band pass filtered the data in each

242 subset of array with 3 or more stations using the frequency band $0.01-f_{\max}$ before rotation
243 and strain derivation.

244

245 **4 Results**

246 In the inversions, shear strains and rotations are determined from ground displacement,
247 therefore we removed the instrument response and trend and integrated the recording to
248 ground displacement using Seismic Analysis Code (SAC) (Goldstein & Snoke, 2005).
249 The data quality is very good, and the waveforms are very similar. Fig. 3(a) shows the
250 displacement waveform of station NA06 filtered at different pass bands with a fixed low-
251 cut frequency of 0.01 Hz and variable high cut frequency, which is denoted at the left y
252 axis for each trace. Fig. 3(b) shows the displacement waveforms of different stations
253 filtered at a pass band of 0.01 to 0.08 Hz. The waveforms are one hour long and initiate at
254 the Tohoku earthquake origin time. The arrival times of P, S, and Rayleigh waves of the
255 mainshock and the estimated P arrival of the 2011/03/11 UTC 06:15 M_w 7.9 aftershock
256 denoted by grey lines in Fig. 3 are theoretical times estimated using the iasp91 model
257 (Kennett & Engdahl, 1991). For comparison, the raw data of station NA06 is shown at
258 the top of Fig. 3(a). The waveform showed large ground displacement during the surface
259 wave: the maximum ground displacement of the unfiltered waveform at NA06 was about
260 3.9 cm and the maximum ground displacement of the filtered waveform at NA06 reached
261 3.2 to 3.3 cm varying with the filter band.

262

263 To see if there are different site effects in the array or other factors affecting the
264 inversions, we examined different combinations of available seismic stations. All

265 configurations are listed in Table S2. We also show the horizontal footprint extent and
 266 corresponding maximum frequency for each inversion. The condition number is
 267 determined by $A^T C_d^{-1} A$ in equation A5 of Spudich et al. (1995) and is associated with the
 268 covariance of the displacement differences. The condition numbers of the inversions were
 269 high when the stations in the subarray were aligned with or orthogonal to the direction of
 270 long axes of the array footprint, i.e., when the array configuration became more linear.
 271 Because a high condition number may give a less robust result, the inversions using
 272 subarrays with high condition number were then excluded from our following analysis.
 273 The maximum frequencies used in Fig. 3(a), 0.08, 0.88, 2.3, and 0.66, represent the high-
 274 cut frequencies applied for the different footprints of subarrays with 6, 5, 4, and 3 stations,
 275 respectively. These representative subarrays are highlighted in Table S2.

276

277 Fig. 4 shows the time series of shear strain, dilation, rotation, and misfit ratio for the
 278 representative subarrays highlighted in Table S2. The stations in the subarray used in the
 279 calculation were [NA04, 06, 07], [NA01, 04, 05, 06], [NA01, 04, 05, 06, 07], and [NA01,
 280 04, 05, 06, 07, NAO05] from the top window to the bottom window. The misfit ratio is

281 explained in Spudich et al. (1995) and is formed as $M = \frac{\sum_{i=1}^N |\mathbf{m}^i|}{\sum_{i=1}^N |\mathbf{d}^i|}$, where

282 $\mathbf{m}^i = \mathbf{d}^i - \mathbf{A}^i \tilde{\mathbf{p}}$ is the misfit vector and \mathbf{d}^i is the data vector. The inversions from different
 283 subarray configurations give comparable time series except for the one using six stations
 284 with a very large footprint. Despite the minor differences, the maximum shear strain and
 285 dilation occurred at about same time (e.g., at 692, 718, and 803 sec). In contrast, the
 286 occurrence of maximum rotation differed for each inversion, showing spatial variations.

287

288 The tremors triggered by the 2011 M_w 9.0 Tohoku earthquake and its M_w 7.9 aftershock
289 recorded at the Nanao array are shown in Fig. 5. The triggered tremors were identified as
290 waveforms showing extended durations of higher frequency signal with amplitudes of 10^{-7}
291 m or greater when the teleseismic trains were passing by. More than ten bursts were
292 recognized. The time windows of the tremors are listed in Table S3 and denoted in Fig. 5
293 by the grey stripes. It is notable that the amplitude of the tremor at NA04 was smallest
294 among all the stations and the tremors recorded at NA05 and NA06 showed clearer
295 signals.

296

297 The spatial variation of the shear strain, dilation, and rotation (Fig. 6a and Fig. 6b) show
298 that the region around the stations NA01, 04, 05, and 06 went through one order of
299 magnitude higher deformation, compared with other array stations further away, during
300 the investigation time. Given the time windows of the tremors, we picked the maximum
301 shear strain, dilation, and rotation for each tremor considering different subarray
302 configurations and plotted the maximum shear strain, dilation, and rotation on the mass
303 center of each subarray. Here we assume the rotation and strain derivations are the
304 average values over the subarray used and thus are located in the mass center of each
305 subarray geometry. Fig. 6a and Fig. 6b show the local maximum shear strain and dilation
306 and the rotations in three components during tremors 1, 3, 7, and 9. Note that the
307 subarrays used here were subsets of four or five stations and the subarrays that yielded
308 condition numbers larger than 200 were not included. The inversions using only three
309 stations were not included because the results might not be as robust. The locations of

310 mass centers (centroids) from the different station configurations were concentrated in
311 three regions. The mass center of stations NA01, 04, 05, and 06 was taken as the
312 reference point (red target in Fig. 6a, b). The values of shear strain, dilation, and rotation
313 tended to be larger around the reference point compared with the sites southwest of the
314 reference point. The dilation and horizontal dilation at each location showed a similar
315 trend and were proportional to each other.

316

317 Large dilations, not rotation or strain, correlate better with tremor occurrence. However,
318 this can be site-dependent. We chose the subarrays giving maximum shear strain during
319 tremor 3 in each region to investigate the temporal relation between shear strain, dilation,
320 and rotation and distance (Fig. 6c). The distances were the horizontal distances between
321 the mass centers of the arrays and the reference point. The trend of dilation and shear
322 strain generally correlated with the teleseismic train; the value started to increase after the
323 P wave passed through (tremor 1 and tremor 6) and reached its maximum after the
324 surface wave passed through (tremor 3 and tremor 7). In addition, the dilation and shear
325 strain are affected by the distance between the centroid and reference point during tremor
326 1 to tremor 9, while rotation is less affected.

327

328 **5 Discussion and conclusions**

329 The Tohoku earthquake teleseismic wave caused large ground motion over whole Taiwan
330 region and triggered many tremors in Nanao but not elsewhere. To better understand the
331 mechanism of dynamic triggering, we examined the velocity waveform from high
332 sensitivity seismometer of Nanao array in different frequency bands and utilized the

333 CWT to study the time-frequency sequence (Fig. 2). From the velocity waveforms and
334 CWT spectrograms, we can identify the tremors and find only some of them have
335 abnormal high energy in high frequency. Fig. 2(a), (b) and Fig. S1-S3 showed that there
336 have been ambient tremors occurred before the Tohoku earthquake and some of them had
337 high energy radiated to high frequency up to larger than 10 Hz. These high frequency
338 tremors were generally associated with VLF events. When the teleseismic wave arrived
339 Nanao, the tremor was triggered (Fig. 2c, 2d, Fig. 5, and Fig. S8). We visually identified
340 10 triggered tremors in one-hour long teleseismic wave trains. To better recognize the
341 triggered tremor, we decomposed the HHZ velocity waveforms to several intrinsic mode
342 functions (IMFs) using empirical mode decomposition (EMD) (Fig. S8). The IMF1
343 resolved the high frequency component that is representative of the tremor we observed
344 in the spectrogram. The instantaneous frequency and energy derived from Hilbert-Huang
345 transform (HHT) revealed that the triggered tremors in the P wave phase may be a cluster
346 of tremors. For the convenience of discussion, we will still name the cluster of tremors in
347 P phase “tremor 1”.

348

349 To study the triggering mechanism and the necessary conditions for triggering, we
350 attempted to locate the tremors, and investigated the six months of seismicity around the
351 Nanao region after the Tohoku earthquake and the spatiotemporal variation of strain and
352 dilation. We tried to determine the rough tremor locations by performing beamforming
353 frequency-wavenumber (FK) analysis using the time span listed in Table S3 and array
354 seismic waveforms. Only tremors 1, 3, 7, and 9 had consistent back azimuths even using
355 different filter bands (Fig. 7a). The color bar corresponds to the sum of the relative power

356 in gridded bins defined by back azimuth and slowness. The back azimuths of tremors 2,
357 4-6, 8, and 10 could not be explicitly determined because the arrival times of the tremors
358 did not show regular moveout but shifted between the stations, implying that the far-field
359 plane wave assumption is not valid, even for this small array. Taking the window of
360 tremor 3 (left panel of Fig. 5c), the envelopes of the waveforms showed an abnormal
361 moveout from NA06 to NA05 for tremor 3 during which the apparent velocities were
362 14.07 m/s (NA06 to NA04), 110 m/s (NA04 to NA01), and 38.57 m/s (NA01 to NA05).
363 The envelope of tremor 7 (right panel of Fig. 5c) showed a reverse moveout direction and
364 the apparent velocity accelerated from 90 m/s (NA05 to NA01), 220 m/s (NA01 to
365 NA04), to 380 m/s (NA04 to NA06). The time series of instantaneous frequency and
366 energy (room-in window of Fig. S8) also showed clear time shifts of tremor 2 between
367 the stations. The large moveout and the varying apparent velocity imply that multiple
368 sources may have been moving slowly within the footprint of this array.

369

370 We propose that the waveforms are generated by moving/dynamic sources. Some sources
371 may be located within the footprints of the array, while others with consistent FK back
372 azimuth direction are outside of the array. However, it is not clear how far away these
373 outside events are. The displacement waveforms of broadband seismograms from the
374 Central Weather Bureau Broadband Seismic Network (CWBBB) (Shin et al., 2013) and
375 the Broadband Array in Taiwan for Seismology (BATS) showed no tremor signal,
376 demonstrating that the sources of the tremors are very close to the array (Fig. S9), and not
377 detectable by regional seismic networks. At least, no tremors were triggered near these
378 CWBBB and BATS stations. The moveout difference and moving sources within the

379 footprint of the array made the location of the tremors hard to identify; only the projected
380 location of tremor 7 was successfully identified (red cross in Fig. 7a) through FK analysis
381 using the HHZ component data of NA04, 06, 07, and NANB (red waveforms in Fig. 5b)
382 and HLZ component of array data (black waveforms in Fig. 5b).

383

384 The Nanao array is located at the tip of the collision of the Philippine Sea Plate and the
385 Eurasian Plate, where the long-term deformation changes from contraction in the south to
386 extension in north. The interaction of extension and compression might create an
387 environment of high stress gradient and provide the opportunity for creating openings
388 along pre-existing cracks or faults. The fluid came from dehydration of the slab and its
389 edge may propagate along these pre-existing cracks or faults and trigger tremors. The
390 strain inversion result (Fig. 6) showed that the block body beneath the array has strongly
391 deformed during the teleseismic wave, especially the dilation component. The maximum
392 dilation obtained during tremor 3 was larger than 10^{-6} and the maximum dilation during
393 the other tremors were all larger than 10^{-8} . These deformations played a key role in the
394 mechanism of tremor triggering. Miyazawa and Mori (2006) found deep low-frequency
395 seismic tremors beneath Japan triggered by the 2004 Sumatra-Andaman M9.2 earthquake
396 and demonstrated that volumetric dilation larger than $\sim 10^{-8}$ was the predominant factor
397 for triggering caused by fluid. Following their findings and the particular geological
398 setting of the Nanao array, next we discuss the potential sources of the crustal fluids in
399 Nanao.

400

401 A seismic tomographic study by Lin et al. (2004) found a low V_s but high V_p/V_s sausage-
402 like body, and they interpreted it as being the result of the dehydration process from the
403 subducting Philippine Sea Plate and its edge. Part of the H₂O-rich component and/or melt
404 may rise up from the sausage-like body through veins and/or narrow conduits to very
405 shallow depths. The sausage-like bodies found by Lin et al. (2004) ranged from 20 to 100
406 km in depth and the location of the shallowest partial melt body is near the Nanao region
407 (Fig. 7b). We projected the six months of northeastern Taiwan seismicity following the
408 Tohoku earthquake onto the NS-EW direction, NS-Vertical direction, and EW-Vertical
409 direction (Fig. 7a). A typical NW subducting slab (grey dash line in Fig. 7a) and a
410 seismic gap beneath the Nanao array extending toward southwest (blue dash line in Fig.
411 7a) could be observed. However, at shallow depth, a NE dipping seismicity is found in
412 the top part of the Philippine Sea Plate near Nanao. Active seismicity in the depth range
413 between 10 km and 18 km on the slab correlates with brittle fractures and the sausage-
414 like body identified by Lin et al. (2004) with low V_s and high V_p/V_s showed rheological
415 property changes beneath 20 km (Yeats, 1997; Zhamaletdinov, 2019). The seismicity
416 deeper than 20 km shows different patterns, possibly related to more ductile deformation.
417 Lin et al. (2004) argued that dehydration along the subducting oceanic slab may provide a
418 fluid source (Seno et al., 2001; Hacker et al., 2003; Yamasaki & Seno, 2003) and the
419 fluids probably propagated upward along the slab until they met the brittle ductile
420 transition (BDT) zone.

421

422 To generate tremors with such large a moveout, it might also be necessary to have large
423 volumes of fluid and even a heat source. The fluids might come from the subducting

424 Philippine Sea Plate, and also partial melts from the subducted slab. Extensive heat
425 sources from depth might also be needed to help mobilize the fluid. There are several hot
426 springs near Nanao. Pore space reduction in sediments on the incoming subducting slab,
427 along with the illite-smectite transition, provide water sources from shallow depths. In
428 addition, partial melts from the slab might provide an additional fluid source in this
429 region, particularly along the edge of the slab. Finally, the BDT zone at 20 km depth
430 might control the fluid circulation; the decreasing permeability in the deeper ductile zone
431 can affect heat and fluid transfer along the propagation path (Driesner & Geiger, 2007;
432 Weis et al., 2012; Violay et al., 2015). The lack of continuous and high sampling rate
433 groundwater level and ground temperature data in Nanao prevent us from directly
434 validating the above hypothesis.

435

436 However, the scenarios obtained from laboratory experiments of fluid-induced seismicity
437 and hydraulic fracturing experiments (Benson et al., 2008; Bakker et al., 2016; Benson et
438 al., 2020) might be an analog to our results. In the laboratory experiment of Benson et al.
439 (2008), high fluid flow (turbulence) could be induced by rapidly venting a high-pressure
440 pore fluid (water), and could generate a clear swarm of acoustic emission, linked to the
441 damage zone. The Nanao tremors show similar waveforms to the acoustic emission from
442 fluid movement due to fluid depressurization at elevated temperatures, which implies that
443 large volumes of fluid and a heat source might be needed. Especially the tremor 1 of
444 clustered tremors triggered by the P wave of Tohoku earthquake showed a high similarity
445 with the swarm of acoustic emission. Bakker et al. (2016) proposed that a rapid increase
446 in pore pressure due to applied stress and heat can lead to tensile fracturing. The resulting

447 fractures will allow a large amount of fluid to move in a relatively short time scale. The
448 time histories of strain and dilation derived from the teleseismic waveform show a similar
449 pattern (left panel of Fig. 4) to the time function of overpressure derived from
450 experiments (right panel of Fig. 4), from the time indicated by the red arrows in Fig. 4.
451 The timing is notable because a drop of overpressure in the early stage of the experiment,
452 which brought up the acoustic emissions and oscillation of overpressure, can be
453 correlated with crustal dilation following the P wave prior to the occurrence of the
454 tremors.

455

456 The seismicity distribution over the six months following the Tohoku earthquake (Fig.
457 7a), showed a seismic gap extending southwest from the Nanao array (blue dashed line in
458 Fig. 7a). The seismic gap might present a potential fracture that may allow the fluid flow
459 to propagate rapidly. The orientation of the back azimuths of the tremors agrees with the
460 layout of the seismic gap, similar to the result of the experiment in Bakker et al. (2016)
461 that showed that the back azimuths of acoustic emissions were aligned with the fracture
462 orientation. Thus, we propose a model as illustrated in the schematic diagram (Fig. 7c).
463 The additional heat from the warm fluids originated from dehydration of the subducting
464 oceanic slab or mantle flow processes around the edge of the slab, propagated upward,
465 and elevated the temperature (and thus the pressure). The dilation following the P wave
466 of the Tohoku earthquake perturbed the pore pressure and activated rapid fluid flow, as
467 shown in the apparent differential moveout observed inside the Nanao array for some of
468 the tremors. The fluid may propagate downward along the fracture (seismic gap) due to
469 gravity accompanied by the turbulence of the fluid. The fluid participating in the

470 turbulence may come from the crust and dehydration, and the temperature and pressure
471 may be key factors for the mobile power of turbulence.

472

473 In summary, the tremors triggered by the M9.0 Tohoku earthquake were found to occur
474 at the collision edge, northeast of Taiwan, by utilizing the Nanao array. The tremors are
475 in the vicinity of the array, but not in other places in Northern Taiwan. We compared our
476 findings to laboratory experiments, and suggest that the triggering mechanism of tremors
477 can be explained by decompression of pore fluid pressure and fluid-rock. We applied
478 Nanao array data using the method of Spudich et al. (1995) and Spudich and Fletcher
479 (2008, 2009) to derive 10^{-6} to 10^{-8} strain and dilation time series, to be correlated with the
480 tremor occurrences. Through different station configurations used in the inversions, we
481 illustrated the spatiotemporal variation of the deformation and triggering thresholds for
482 this particular event. The hybrid reaction of fluid triggered these tremors. The
483 dehydration of the subducting oceanic slab based on Lin et al. (2004) or the mantle flow
484 around the edge of the slab may provide sources of additional fluid and heat for fluid
485 saturated in crust, thus triggering the tremors when teleseismic waves pass through. This
486 is among the first field observations from a small aperture array for dynamically triggered
487 tremors above the edge of subducting slab, suggesting such a geological setting might
488 merit further dynamic triggering studies.

489

490 **Data and Resources**

491 The data that support the findings of this study are available at
492 <https://doi.org/10.7910/DVN/PNPEXA>. Further data of the Nanao array and the

493 conditions for access will be available at the Taiwan Earthquake Research Center (TEC)
494 Data center at <http://tecdc.earth.sinica.edu.tw>.

495

496 **Acknowledgements**

497 We thank TEC for providing the instruments. We thank Dr. A. Song, Editor R.
498 Abercrombie, and Associate Editor for their valuable suggestions and comments. The
499 Nanao array was designed and initiated by W.-C. Chi with Mr. W.S. Liu installed the
500 array. Dr. Chi thanks the able help from IES engineers led by Mr. C.C. Liu and Dr. C. J.
501 Lin. This project is partially funded by Institute of Earth Sciences, Academia Sinica and
502 MOST of Taiwan.

503

504 **References**

505 Angelier, J. (1986). Geodynamics of the Eurasia-Philippine Sea Plate boundary: Preface.
506 *Tectonophysics*, 125, IX–X. [https://doi.org/10.1016/0040-1951\(86\)90003-X](https://doi.org/10.1016/0040-1951(86)90003-X)

507

508 Bakker, R. R., Fazio, M., Benson, P. M., Hess, K. U., & Dingwell, D. B. (2016). The
509 propagation and seismicity of dyke injection, new experimental evidence. *Geophysical*
510 *Research Letters*, 43, 1876–1883. <https://doi.org/10.1002/2015GL066852>

511

512 Benson, P. M., Austria, D. C., Gehne, S., Butcher, E., Harnett, C. E., Fazio, M., Rowley,
513 P., & Tomas R. (2020). Laboratory simulations of fluid-induced seismicity, hydraulic
514 fracture, and fluid flow. *Geomechanics for Energy and the Environment*, 24, 100169.
515 <https://doi.org/10.1016/j.gete.2019.100169>

516

517 Benson, P. M., Vinciguerra, S., Meredith, P., & Young, R. (2008). Laboratory simulation
518 of volcano seismicity. *Science*, 322:249–252. <https://doi.org/10.1126/science.1161927>

519

520 Beroza, G.C., & Ide, S. (2011). Slow earthquakes and nonvolcanic tremor. *Annual*
521 *Review of Earth and Planetary Sciences*, 39:271–296. [https://doi.org/10.1146/annurev-](https://doi.org/10.1146/annurev-earth-040809-152531)
522 [earth-040809-152531](https://doi.org/10.1146/annurev-earth-040809-152531)

523

524 Brodsky, E. E., Roeloffs, E., Woodcock, D., Gall, I., & Manga, M. (2003). A mechanism
525 for sustained groundwater pressure changes induced by distant earthquakes. *Journal of*
526 *Geophysical Research*, 108(B8), 2390. <https://doi.org/10.1029/2002JB002321>

527

528 Brodsky, E., Sturtevant, B., & Kanamori, H. (1998). Earthquakes, volcanoes, and
529 rectified diffusion. *Journal of Geophysical Research*, 103(B10), 23827–23838.
530 <https://doi.org/10.1029/98JB02130>

531

532 Buehler, J. S., & Shearer, P. M. (2015). T phase observations in global seismogram
533 stacks. *Geophysical Research Letters*, 42, 6607–6613.
534 [https://doi:10.1002/2015GL064721](https://doi.org/10.1002/2015GL064721)

535

536 Chao, K., Peng, Z., Gonzalez-Huizar, H., Aiken, C., Enescu, B., Kao, H., Velasco, A. A.,
537 Obara, K., & Matsuzawa, T. (2013). A global search for triggered tremor following the

538 2011 Mw 9.0 Tohoku earthquake. *Bulletin of the Seismological Society of America*,
539 103(2B), 1551–1571. <https://doi.org/10.1785/0120120171>

540

541 Chao, K., Peng, Z., Wu, C., Tang, C.-C., & Lin, C.-H. (2012). Remote triggering of non-
542 volcanic tremor around Taiwan. *Geophysical Journal International*, 188(1), 301–324.
543 <https://doi.org/10.1111/j.1365-246X.2011.05261.x>

544

545 Chi, W.-C., Dreger, D., & Kaverina, A. (2001). Finite source modeling of the 1999
546 Taiwan (Chi-Chi) Earthquake derived from a dense strong motion network, *Bulletin of*
547 *the Seismological Society of America*, 91(5), 1144 – 1157.
548 <https://doi.org/10.1785/0120000732>

549

550 Chi, W.-C., Lee, W. H. K., Aston, J. A. D., Lin, C.-J., & Liu, C.-C. (2011). Inversion of
551 ground motion data from a seismometer array for rotation using a modification
552 of Jeager’s method. *Bulletin of the Seismological Society of America*, 101(6), 3105 –
553 3109. <https://doi.org/10.1785/0120100204>

554

555 Chiu, H. C., Yeh, Y. T., Ni, S. D., Lee, L., Liu, W. S., Wen, C. F., & Liu, C. C. (1994). A
556 new strong-motion array in Taiwan: SMART-2. *Terrestrial Atmospheric and Oceanic*
557 *Sciences*, 5, 463–475. [https://doi: 10.3319/TAO.1994.5.4.463\(T\)](https://doi:10.3319/TAO.1994.5.4.463(T))

558

559 Donner, S., Lin, C.-J., Hadziioannou, C., Gebauer, A., Vernon, F., Agnew, D. C., Igel, H.,
560 Schreiber, U., & Wassermann J. (2017). Comparing direct observation of strain, rotation,

561 and displacement with array estimates at Piñon Flat Observatory,
562 California. *Seismological Research Letters*, 88(4), 1107–1116.
563 <https://doi.org/10.1785/0220160216>
564
565 Dreger, D. S., Tkalčić, H., & Johnston, M., (2000). Dilational processes accompanying
566 earthquakes in the Long Valley Caldera. *Science*, 288(5463), 122-125.
567 <https://doi.org/10.1126/science.288.5463.122>
568
569 Driesner, T., & Geiger, S. (2007). Numerical simulation of multiphase fluid flow in
570 hydrothermal systems, in A. Liebscher, C. A. Heinrich (Eds.), *Fluid-fluid interactions,*
571 *Reviews in Mineralogy & Geochemistry* (Vol. 65, pp. 187–212). Chantilly, VA:
572 Mineralogical Society of America. <https://doi.org/10.2138/rmg.2007.65.6>
573
574 Foulger, G. R., Julian, B. R., Hill, D. P., Pitt, A. M., Malin, P. E., & Shalev, E., (2004).
575 Non-double-couple microearthquakes at Long Valley caldera, California, provide
576 evidence for hydraulic fracturing. *Journal of Volcanology and Geothermal*
577 *Research*, 132(1), 45–71. [https://doi.org/10.1016/S0377-0273\(03\)00420-7](https://doi.org/10.1016/S0377-0273(03)00420-7)
578
579 Goldstein, P., & Snoke, A. (2005). *SAC Availability for the IRIS Community,*
580 Incorporated Institutions for Seismology Data Management Center Electronic Newsletter.
581
582 Gomberg, J. (2001). The failure of earthquake failure models, *Journal of Geophysical*
583 *Research: Solid Earth*, 106(B8), 16253–16263. <https://doi.org/10.1029/2000JB000003>

584

585 Gomberg, J., Beeler, N. M., Blanpied, M. L., & Bodin, P. (1998). Earthquake triggering
586 by transient and static deformation. *Journal of Geophysical Research: Solid Earth*,
587 *103*(B10), 24411–24426. <https://doi.org/10.1029/98JB01125>

588

589 Gomberg, J., Bodin, P., Larson, K., & Dragert H. (2004). Earthquakes nucleated by
590 transient deformations caused by the M 7.9 Denali, Alaska, earthquake. *Nature*, *427*,
591 621–624. <https://doi.org/10.1038/nature02335>

592

593 Gomberg, J., & Johnson, P. (2005). Dynamic triggering of earthquakes. *Nature*, *437*,
594 830. <https://doi.org/10.1038/437830a>

595

596 Gomberg, J., Reasenber, P. A., Cocco, M., & Belardinelli, M. E. (2005). A frictional
597 population model of seismicity rate change. *Journal of Geophysical Research: Solid*
598 *Earth*, *110*(B5), S03. <https://doi.org/10.1029/2004JB003404>

599

600 Gonzalez-Huizar, H., & Velasco, A. A. (2011). Dynamic triggering: Stress modeling and
601 a case study. *Journal of Geophysical Research: Solid Earth*, *116*, B02304.

602

603 Hacker, B. R., Peacock, S. M., Abers, G. A., & Holloway S. D. (2003). Subduction
604 factory 2. Are intermediate-depth earthquakes in subducting slabs linked to metamorphic
605 dehydration reactions?. *Journal of Geophysical Research: Solid Earth*, *108*(B1), 2030.
606 <https://doi.org/10.1029/2001JB001129>

607

608 Hill, D. P. (2008). Dynamic stresses, coulomb failure, and remote triggering. *Bulletin of*
609 *the Seismological Society of America*, 98(1), 66–92. <https://doi.org/10.1785/0120070049>

610

611 Hill, D. P., & Prejean, S. G. (2007). Dynamic triggering, in G. Schubert (Eds.), *Treatise*
612 *on Geophysics* (Second Edition) (Vol. 4, pp. 273–304). Amsterdam,
613 Elsevier. <https://doi.org/10.1016/B978-0-444-53802-4.00078-6>

614

615 Hill, D.P., Pollitz F., Newhall, C. (2002). Earthquake-volcano interactions. *Physics*
616 *Today*, 55(11), 41–47. <https://doi.org/10.1063/1.1535006>

617

618 Hill, D. P., Reasenber, P. A., Michael, A., Arabaz, W. J., Beroza, G., Brumbaugh, D.,
619 Brune, J. N., Castro, R., Davis, S., dePolo, D., Ellsworth, W. L., Gomberg J., Harmsen, S.,
620 House, L., Jackson, S. M., Johnston, M. J. S., Jones, L., Keller, R., Malone, S., Munguia,
621 L., Nava, S., Pechmann, J. C., Sanford, A., Simpson, R. W., Smith, R. B., Stark,
622 M., Stickney, M., Vidal, A., Walter, S., Wong, V., & Zollweg, J. (1993).
623 Seismicity remotely triggered by the magnitude 7.3 Landers, California, earthquake.

624 *Science*, 260(5114), 1617–1623. <https://doi.org/10.1126/science.260.5114.1617>

625

626 Hough, S. E., Seeber, L., & Armbruster, J. G. (2003). Intraplate triggered earthquakes:
627 Observations and interpretation, *Bulletin of the Seismological Society of America*,
628 93(5), 2212–2221. <https://doi.org/10.1785/0120020055>

629

- 630 Huang, B. S. (2003). Ground rotational motions of the 1999 Chi-Chi, Taiwan, earthquake
631 as inferred from dense array observations. *Geophysical Research Letters*, 30(6), 1307.
632 <https://doi.org/10.1029/2002GL015157>
633
- 634 Huang, H.-H., Shyu, J. B. H., Wu, Y.-M., Chang, C.-H. & Chen, Y.-G. (2012).
635 Seismotectonics of northeastern Taiwan: Kinematics of the transition from waning
636 collision to subduction and postcollisional extension. *Journal of Geophysical Research:*
637 *Solid Earth*, 117, B01313. <https://doi.org/10.1029/2011JB008852>
638
- 639 Institute of Earth Sciences, A. S. (1996). *Broadband Array in Taiwan for Seismology*.
640 Institute of Earth Sciences, Academia Sinica, Taiwan. <https://doi.org/10.7914/SN/TW>
641
- 642 Jiang, T., Peng, Z., Wang, W., & Chen, Q.-F. (2010). Remotely triggered seismicity in
643 continental China following the 2008 M_w 7.9 Wenchuan earthquake. *Bulletin of the*
644 *Seismological Society of America*, 100(5B), 2574–2589. <https://doi.org/10.1785/0120090286>
645
- 646 Johnson, P. & Jia, X. (2005). Nonlinear dynamic, granular media and dynamic
647 earthquake triggering. *Nature*, 437, 871–874. <https://doi.org/10.1038/nature04015>
648
- 649 Johnson, C. W., Meng, H., Vernon, F., & Ben-Zion, Y. (2019). Characteristics of ground
650 motion generated by wind interaction with trees, structures, and other surface obstacles.
651 *Journal of Geophysical Research: Solid Earth*, 124, 8519–8539. [https://doi.org/10.1029/](https://doi.org/10.1029/2018JB017151)
652 2018JB017151

653

654 Kennett, B. L. N. & Engdahl, E. R. (1991). Traveltimes for global earthquake location
655 and phase identification. *Geophysical Journal International*, 105(2), 429–465.
656 <https://doi.org/10.1111/j.1365-246X.1991.tb06724.x>

657

658 Lin, J.-Y., Hsu, S.-K., & Sibuet, J. C. (2004). Melting features along the western Ryukyu
659 slab edge (northeast Taiwan): Tomographic evidence. *Journal of Geophysical Research:*
660 *Solid Earth*, 109, B12402. <https://doi:10.1029/2004JB003260>

661

662 Linde, A. T., Sacks, I. S., Johnston, M. J. S., Hill, D. P., & Billham, R. G. (1994).
663 Increased pressure from rising bubbles as a mechanism for remotely triggered seismicity.
664 *Nature*, 371, 408-410. <https://doi.org/10.1038/371408a0>

665

666 Miyazawa, M., & Mori, J. (2006). Evidence suggesting fluid flow beneath Japan due to
667 periodic seismic triggering from the 2004 Sumatra-Andaman earthquake. *Geophysical*
668 *Research Letters*, 33, L05303. <https://doi:10.1029/2005GL025087>

669

670 Obara, K. (2002). Nonvolcanic deep tremor associated with subduction in southwest
671 Japan. *Science*, 296, 1679. doi:[10.1126/science.1070378](https://doi.org/10.1126/science.1070378)

672

673 Obara, K., & Kato, A. (2016). Connecting slow earthquakes to huge earthquakes.
674 *Science*, 353(6296), 253–257. <https://doi:10.1126/science.aaf1512>

675

- 676 Peacock, S. M. (2009). Thermal and metamorphic environment of subduction zone
677 episodic tremor and slip. *Journal of Geophysical Research: Solid Earth*, 114, B00A07.
678 <https://doi:10.1029/2008JB005978>
679
- 680 Peng, Z., & Chao, K. (2008). Non-volcanic tremor beneath the Central Range in Taiwan
681 triggered by the 2001 Mw 7.8 Kunlun earthquake. *Geophysical Journal International*,
682 175(2), 825–829. <https://doi.org/10.1111/j.1365-246X.2008.03886.x>
683
- 684 Perfettini, H., Schmittbuhl, J., & Cochard, A. (2003). Shear and normal load
685 perturbations on a two-dimensional continuous fault: 2. Dynamic triggering. *Journal of*
686 *Geophysical Research: Solid Earth*, 108(B9), 2409.
687 <https://doi.org/10.1029/2002JB001805>
688
- 689 Prejean, S. G., Hill, D. P., Brodsky, E. E., Hough, S. E., Johnston, M. J. S., Malone, S. D.,
690 Oppenheimer, D. H., Pitt, A. M., & Richards-Dinger, K. B. (2004). Remotely triggered
691 seismicity on the United States west coast following the M_w 7.9 Denali fault earthquake.
692 *Bulletin of the Seismological Society of America*, 94(6B), S348.
693 <http://dx.doi.org/10.1785/0120040610>
694
- 695 Seno, T., Zhao, D., Kobayashi, Y., & Nakamura, M. (2001). Dehydration of
696 serpentinitized slab mantle: Seismic evidence from southwest Japan. *Earth Planets and*
697 *Space*, 53, 861–871. <https://doi.org/10.1186/BF03351683>
698

699 Shin, T. C., Chang, C. H., Pu, H. C., Lin, H. W., & Leu, P. L. (2013). The Geophysical
700 Database Management System in Taiwan. *Terrestrial Atmospheric and Oceanic Sciences*,
701 24, 11-18. [http://doi: 10.3319/TAO.2012.09.20.01\(T\)](http://doi:10.3319/TAO.2012.09.20.01(T))

702

703 Shin, T. C., Tsai, Y. B., Yeh, Y. T., Liu, C. C., & Wu, Y. M. (2003). Strong-Motion
704 Instrumentation Programs in Taiwan, in "Handbook of Earthquake and Engineering
705 Seismology" edited by W. H. K. Lee, H. Kanamori, and P. C. Jennings, *Academic Press*,
706 p. 1057-1602.

707

708 Spudich, P., & Fletcher, J. B. (2008). Observation and prediction of dynamic ground
709 strains, tilts, and torsions caused by the M 6.0 2004 Parkfield, California, earthquake and
710 aftershocks derived from UPSAR array observations. *Bulletin of the Seismological*
711 *Society of America*, 98, 1898–1914. <http://doi:10.1785/0120070157>

712

713 Spudich, P., & Fletcher, J. B. (2009). Software for inference of dynamic ground strains
714 and rotations and their errors from short baseline array observations of ground motions.
715 *Bulletin of the Seismological Society of America*, 99, 1480–
716 1482. <http://doi:10.1785/0120080230>

717

718 Spudich, P., Steck, L. K., Hellweg, M., Fletcher, J. B., & Baker, L. M. (1995). Transient
719 stresses at Parkfield, California, produced by the M 7.4 Landers earthquake of June 28,
720 1992: Observations from the UPSAR dense seismograph array. *Journal of Geophysical*
721 *Research*, 100, 675–690. <https://doi.org/10.1029/94JB02477>

722

723 Sun, W.-F., Peng, Z., Lin, C.-H., & Chao, K. (2015). Detecting deep tectonic tremor in
724 Taiwan with a dense array. *Bulletin of the Seismological Society of America*,
725 105(3), 1349–1358. <https://doi.org/10.1785/0120140258>

726

727 Suryanto, W., Igel, H., Wassermann, J., Cochard, A., Schuberth, B., Vollmer, D.,
728 Scherbaum, F., Schreiber, U., & Velifoseltsev, A. (2006). First comparison of array-
729 derived rotational ground motions with direct ring laser measurements. *Bulletin of the*
730 *Seismological Society of America*, 96, 2059–2071. <https://doi.org/10.1785/0120060004>

731

732 Teng, L. S. (1996). Extensional collapse of the northern Taiwan mountain belt. *Geology*,
733 24, 949–952. [https://doi.org/10.1130/0091-7613\(1996\)024<0949:ECOTNT>2.3.CO;2](https://doi.org/10.1130/0091-7613(1996)024<0949:ECOTNT>2.3.CO;2)

734

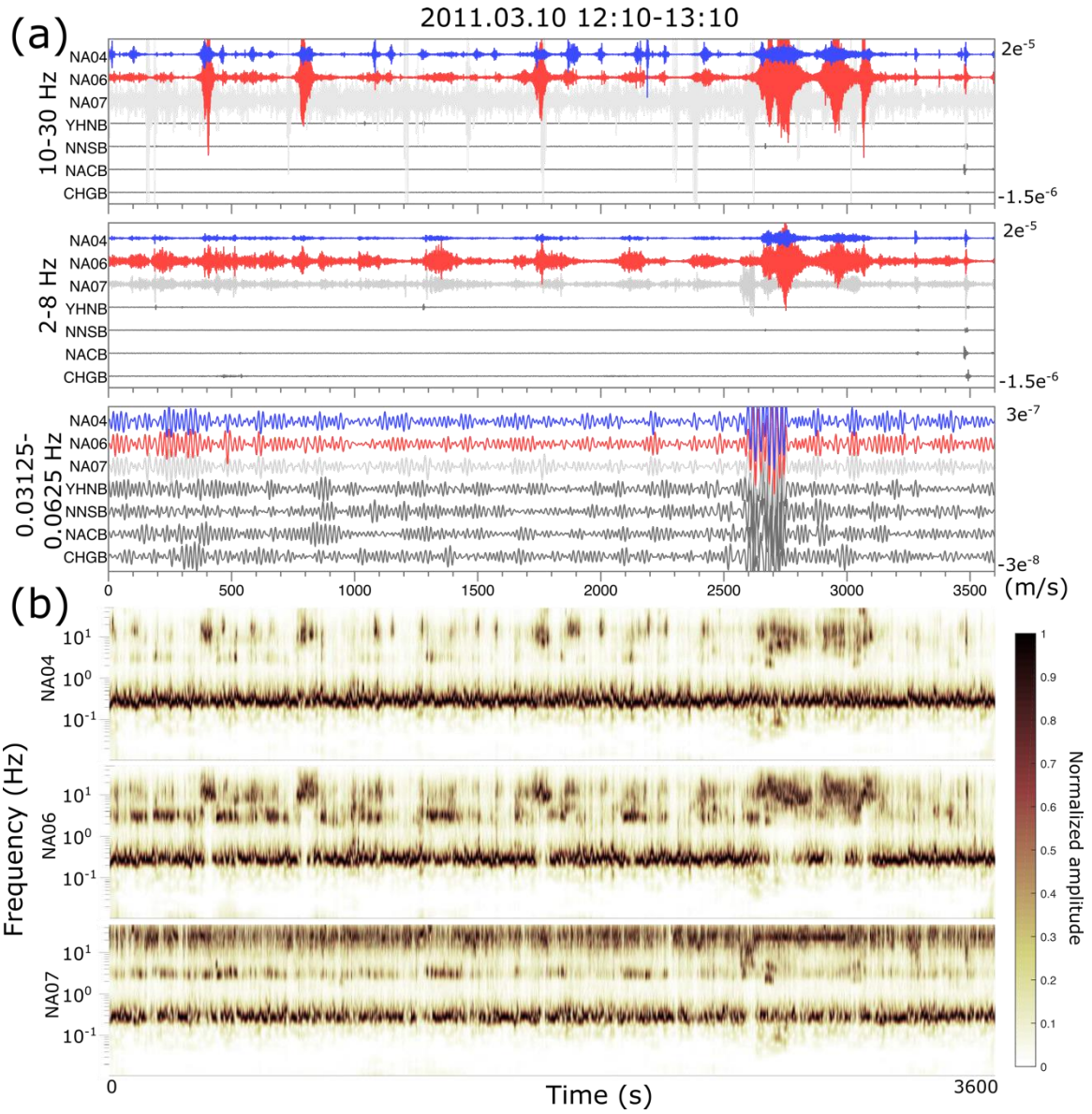
735 Van Avendonk, H. J. A., McIntosh, K. D., Kuo-Chen, H., Lavier, L. L., Okaya, D. A.,
736 Wu, F. T., Wang, C.-Y., Lee, C.-S., & Liu, C.-S. (2016). A lithospheric profile across
737 northern Taiwan: from arc-continent collision to extension. *Geophysical Journal*
738 *International*, 204, 331–346. <https://doi.org/10.1093/gji/ggv468>

739

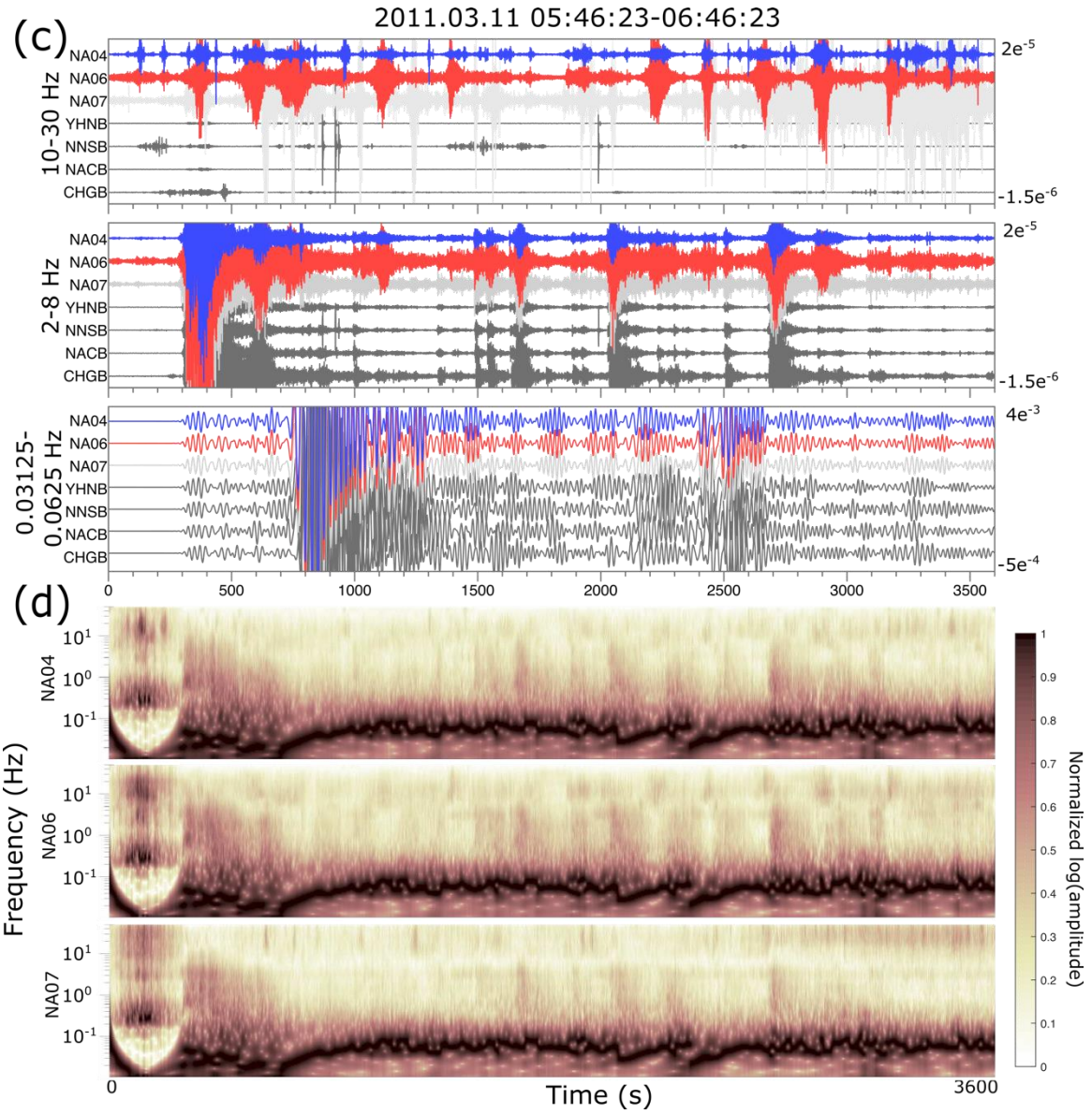
740 Velasco, A. A., Hernandez, S., Parson, T., & Pankow, K. (2008). Global ubiquity of
741 dynamic earthquake triggering. *Nature Geoscience*, 1, 375–
742 379. <https://doi.org/10.1038/ngeo204>

743

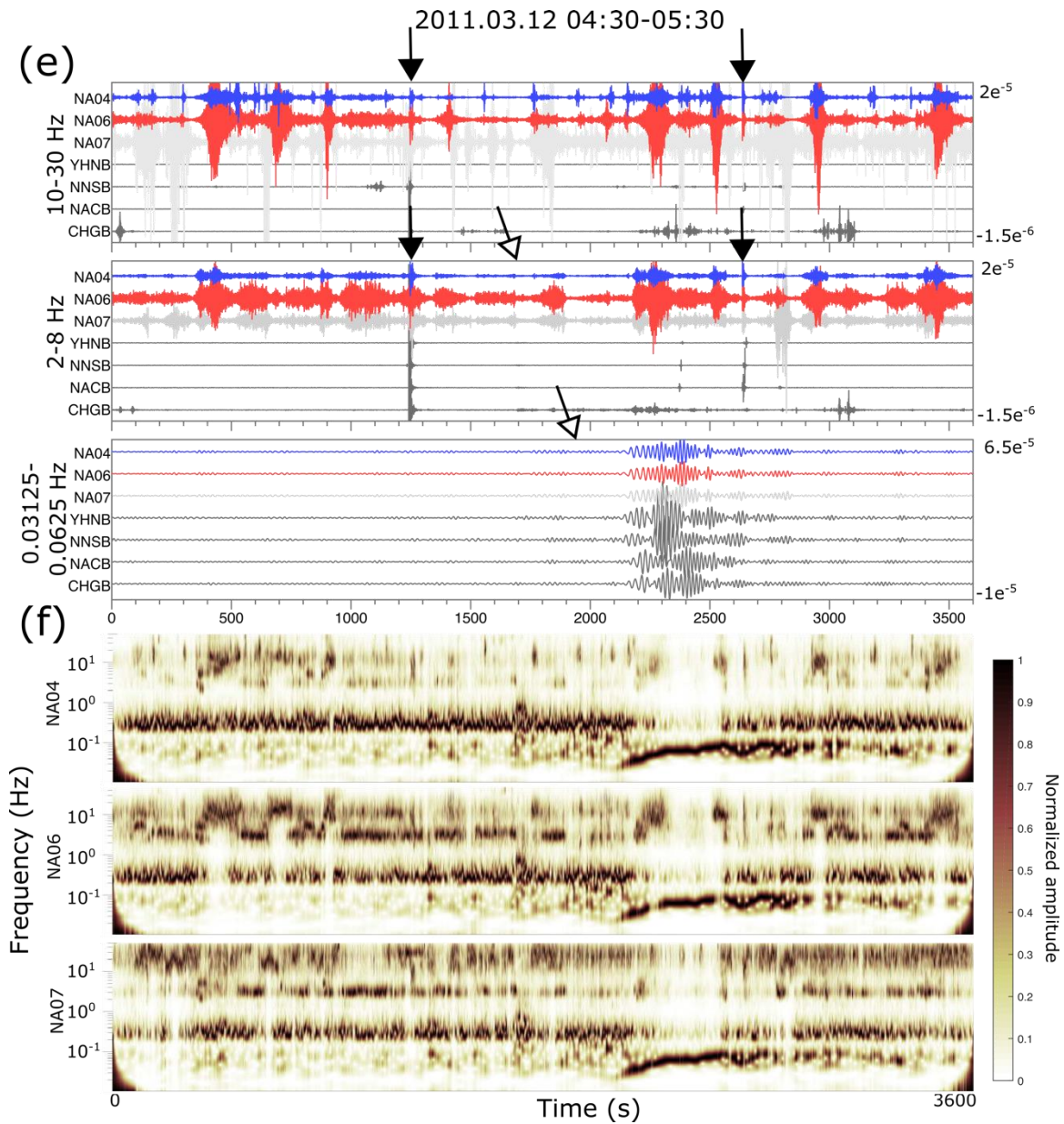
- 744 Violay, M., Gibert, B., Mainprice, D., & Burg, J. P. (2015). Brittle versus ductile
745 deformation as the main control of the deep fluid circulation in oceanic crust.
746 *Geophysical Research Letters*, 42, 2767–2773. [https://doi:10.1002/ 2015GL063437](https://doi.org/10.1002/2015GL063437)
747
- 748 Weis, J. P., Driesner, T., & Heinrich, C. A. (2012). Porphyry-copper ore shells form at
749 stable pressure-temperature fronts within dynamic fluid plumes. *Science*, 338, 1613–1616.
750 [https://doi:10.1126/science.1225009](https://doi.org/10.1126/science.1225009)
751
- 752 Yamasaki, T., & Seno, T. (2003). Double seismic zone and dehydration embrittlement of
753 the subducting slab. *Journal of Geophysical Research*, 108(B4), 2212.
754 [https://doi:10.1029/2002JB001918](https://doi.org/10.1029/2002JB001918)
755
- 756 Yeats, R. S., Allen, C. R., & Sieh, K. E. (1997). *The Geology of Earthquakes*, Oxford
757 Univ. Press, New York.
758
- 759 Zhamaletdinov, A. A. (2019). On the nature of the brittle-ductile transition zone in the
760 Earth's crust (review). In: Zhamaletdinov A., Rebetsky Y. (eds) *The Study of Continental*
761 *Lithosphere Electrical Conductivity, Temperature and Rheology*. SPS 2018. *Springer*
762 *Proceedings in Earth and Environmental Sciences*. Springer, Cham.
763 https://doi.org/10.1007/978-3-030-35906-5_3
764



770



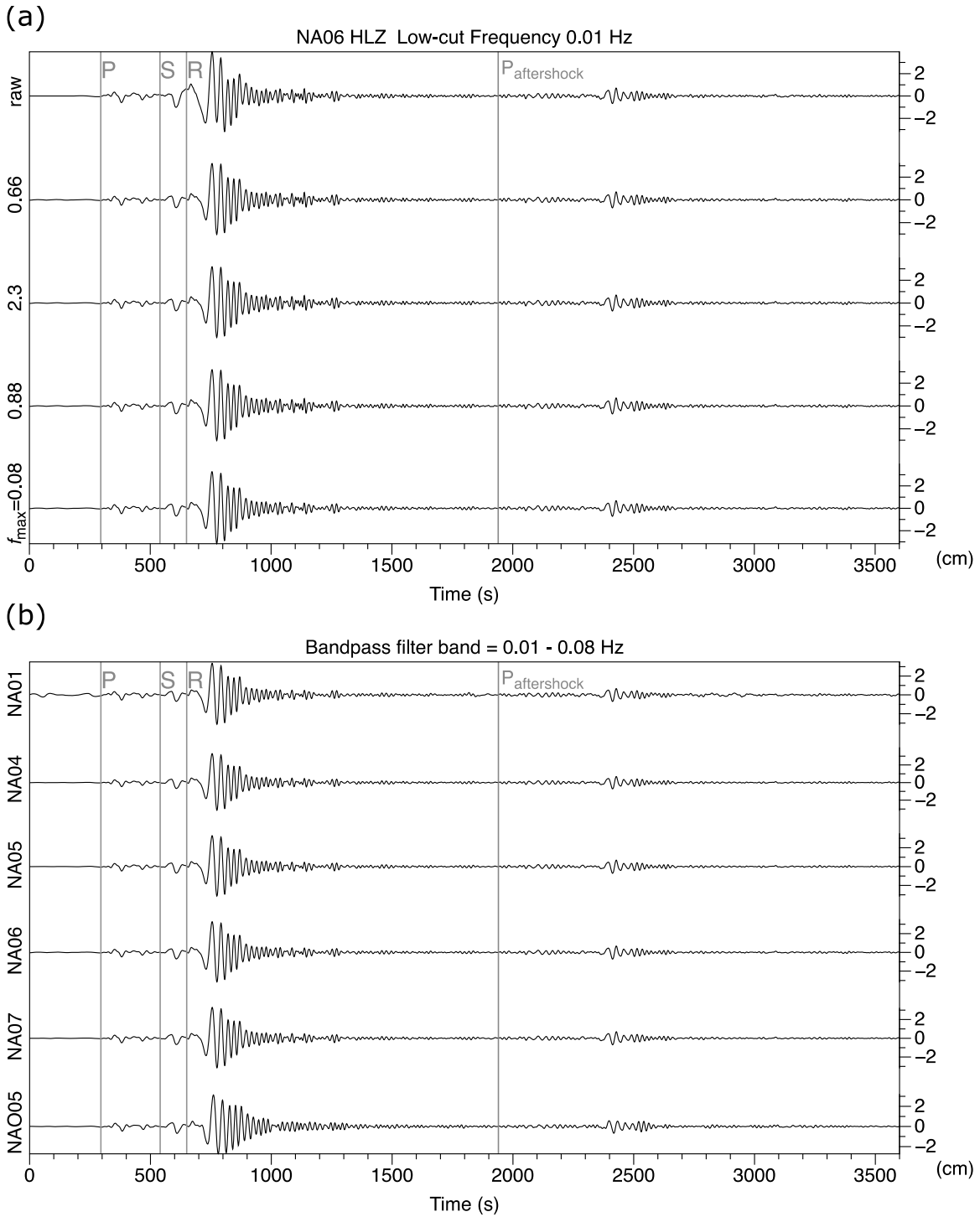
771



772

773 **Figure 2.** The filtered velocity seismograms in vertical component and the CWT
 774 spectrogram in the time period (a) (b) 4-5pm on March 10, (c) (d) 5:46-6:46am on March
 775 11, and (e) (f) 4:30-5:30am on March 12. The filter bands of 10-30 Hz, 2-8 Hz, and
 776 0.03125-0.0625 s (top to bottom) were applied for better recognizing high frequency
 777 tremor, tremor, and very-low-frequency event. The time window in (a) (b) is quieter time
 778 period compared with other pre-seismic periods (e.g. Fig. S1-S3). The 10-30 Hz band-

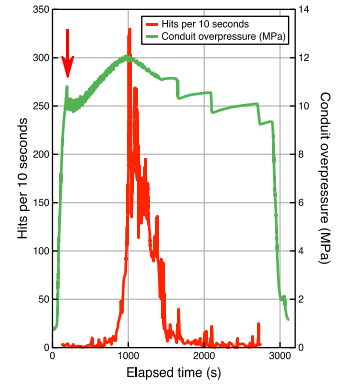
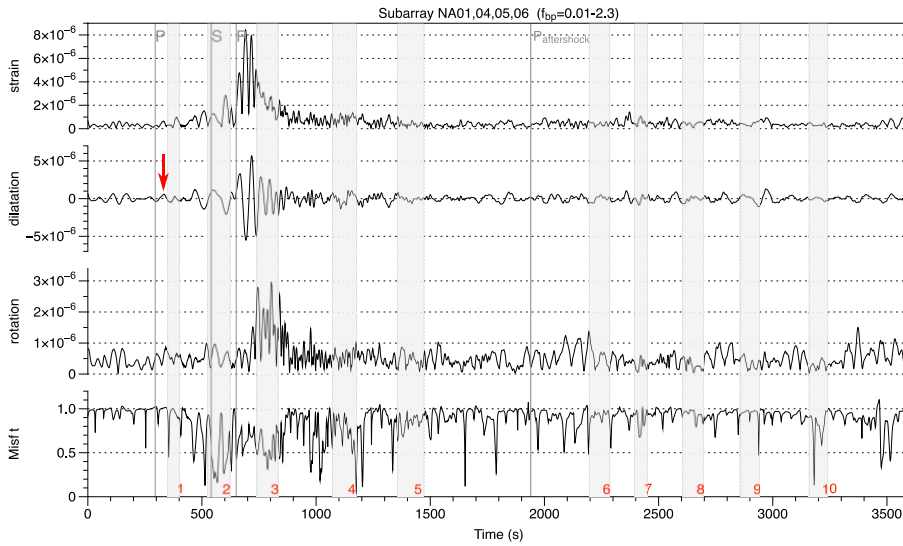
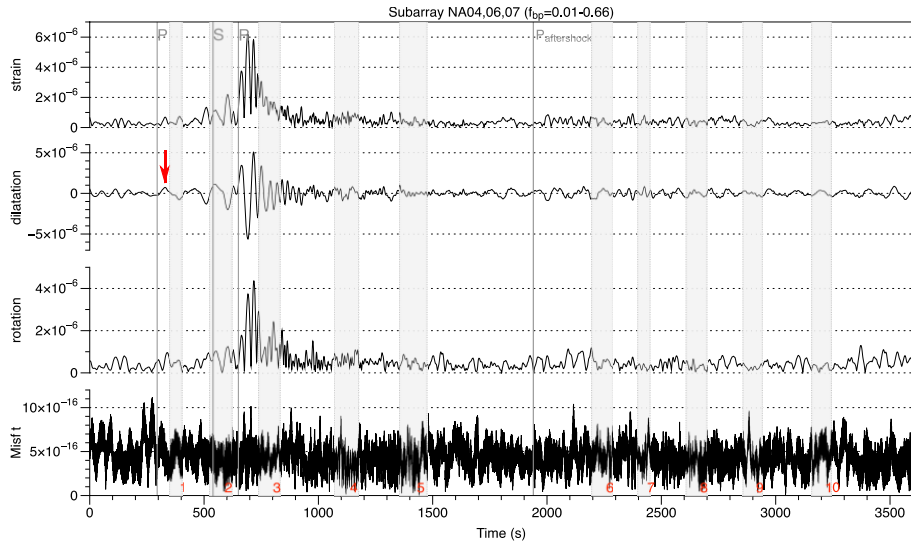
779 pass filtered waveforms share the same amplitude scale with the 2-8 Hz band-pass
780 filtered waveform during all the studying periods while the amplitude scales of 0.03125-
781 0.0625 Hz band pass filtered waveforms are different in (a) (b), co-seismic (c) (d), and
782 post-seismic (e) (f) periods. The hollow arrows and solid arrows indicate the first arrivals
783 of the Tohoku sequence teleseismic and local earthquakes, respectively.



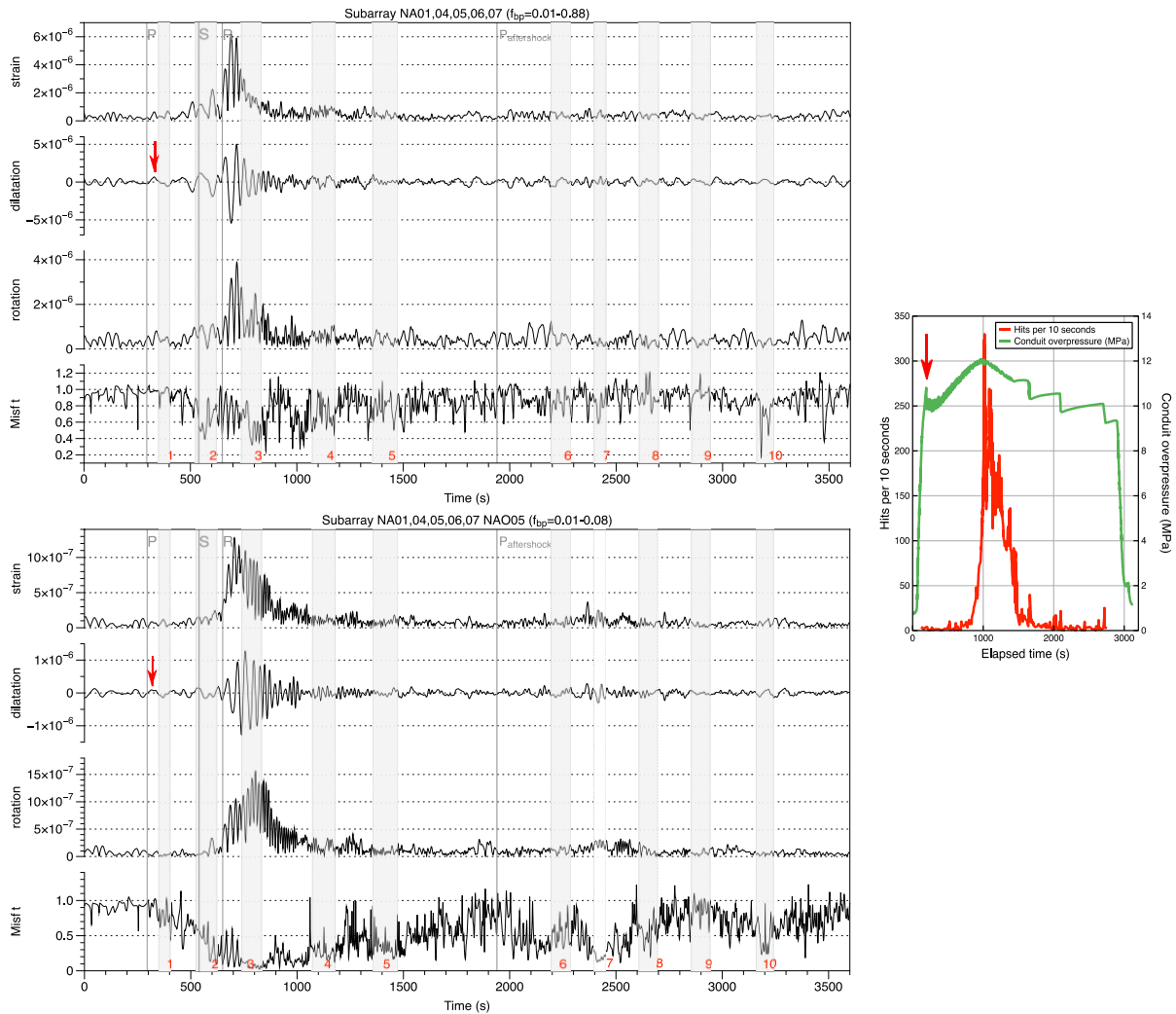
784

785 **Figure 3.** The waveforms applied in Spudich's strain inversion. (a) The seismogram
 786 applied with different filter bands at NA06. The time spans from the occurrence of the
 787 Tohoku earthquake to one hour after. The grey lines denote the estimated arrival times of

788 P, S, and Rayleigh waves of the mainshock and the estimated P arrival of the 2011/03/11
789 UTC 06:15 M_w 7.9 aftershock. The maximum usable frequencies corresponding to
790 different subarray configurations were applied as the high cut frequencies in Butterworth
791 bandpass filter and are denoted at the left y axis, and the right y axis shows the amplitude
792 of displacement. (b) The seismograms bandpass filtered with filter band 0.01 to 0.08 Hz
793 at all six stations.
794



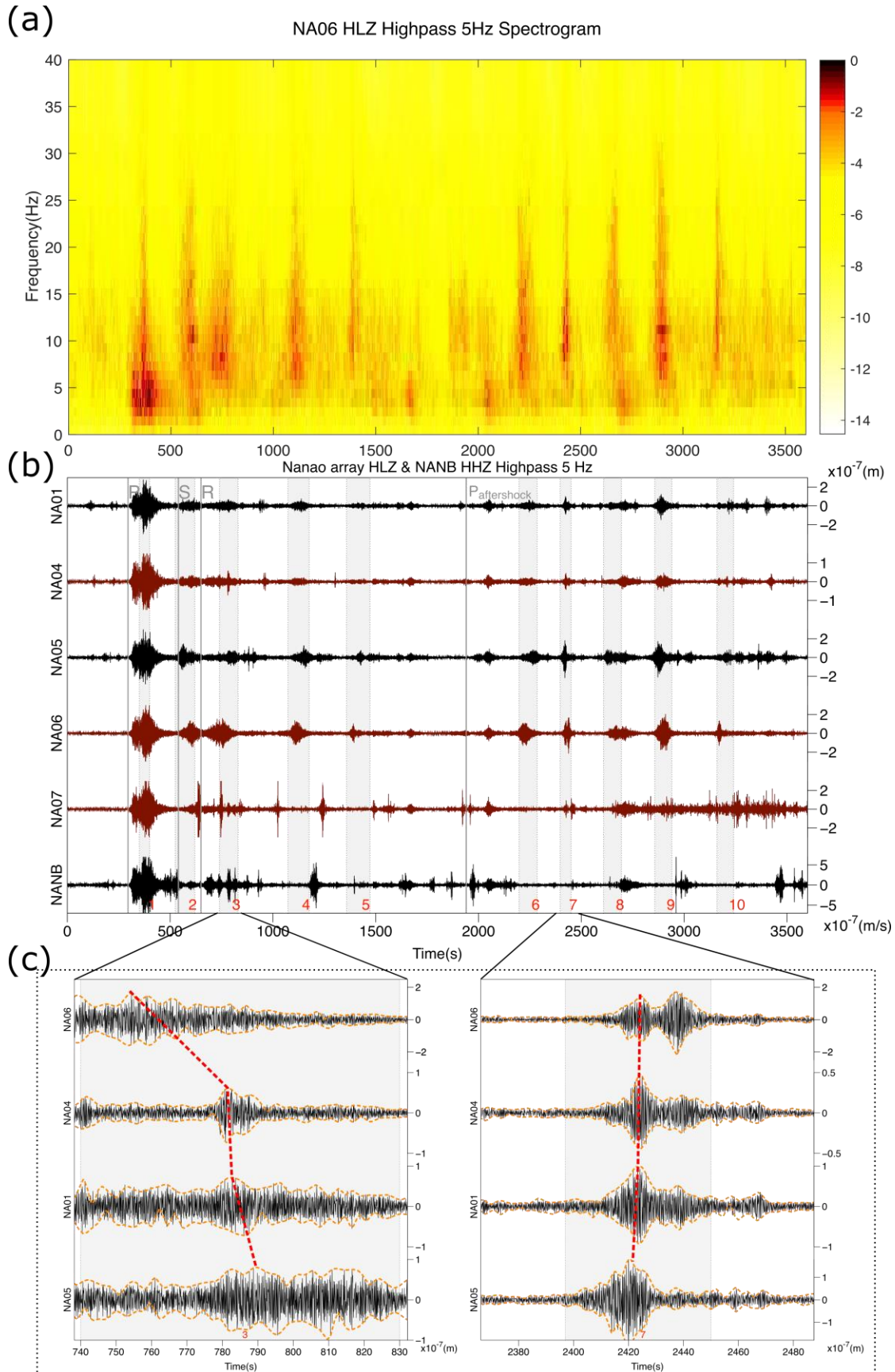
795



796

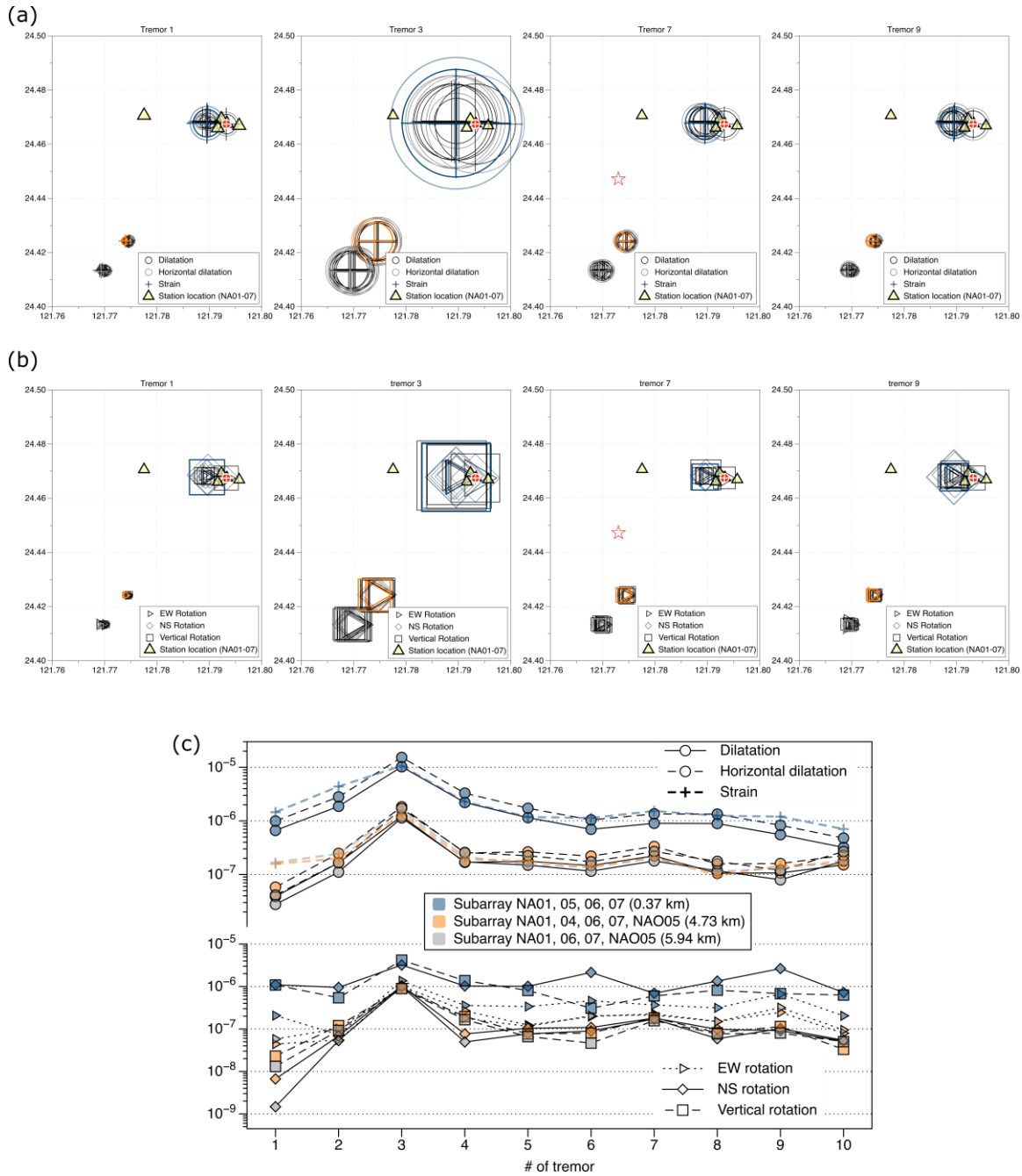
797 **Figure 4.** (Left) Time series of shear strains, dilations, rotations and misfits inferred by
 798 the method of Spudich et al. (1995) using different stations of subarrays. The stations
 799 implemented in the inversion are [NA04, 06, 07], [NA01, 04, 05, 06], [NA01, 04, 05, 06,
 800 07], and [NA01, 04, 05, 06, 07, NAO05] from the top to the bottom. The frequency band
 801 applied for the Butterworth bandpass filter are labeled on each title. The grey lines
 802 indicate the estimated arrival time of the P, S, and Rayleigh waves and the light gray
 803 strips show the tremor durations. (Right) The laboratory experiment results showing the
 804 conduit overpressure and acoustic emission hit count during pressurization of a heated
 805 conduit filled with PMMA (polymethyl methacrylate), modified from Bakker et al.

806 (2016). The red arrows indicate the comparable timing of conduit overpressure drop and
807 occurrence of measurable acoustic emission hits in the experiment and the initial dilation
808 and detected tremors in our study. Also note that the peak at a conduit pressure
809 coinciding with the peak in acoustic emission hit rate as rock failure occur can be linked
810 to the simultaneous peak of dilation and strain.
811



812

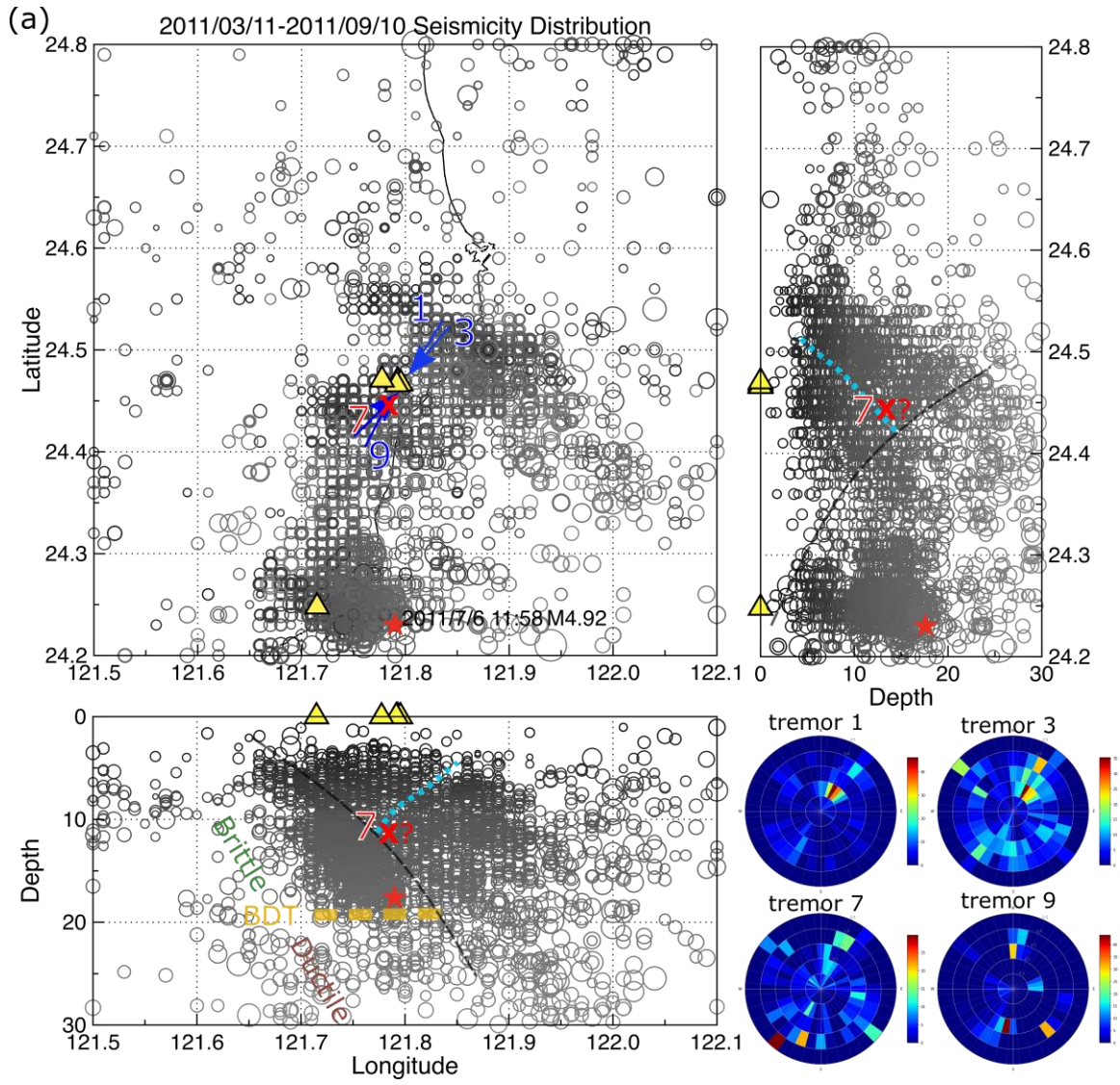
813 **Figure 5.** The tremor triggered by the 2011 M_w 9.0 Tohoku earthquake and its M_w 7.9
814 aftershock recorded at the Nanao array. (a) The spectrogram of 5 Hz high-pass-filtered
815 seismograms at station NA06. (b) The 5 Hz high-pass-filtered seismograms at each
816 station and 10 possible triggered tremors identified by the process described in the text. (c)
817 The zoom-in window of tremor 3 and tremor 7. The orange dashed lines outline the
818 envelopes of the waveforms and the irregular moveout is shown by the red dash line.
819



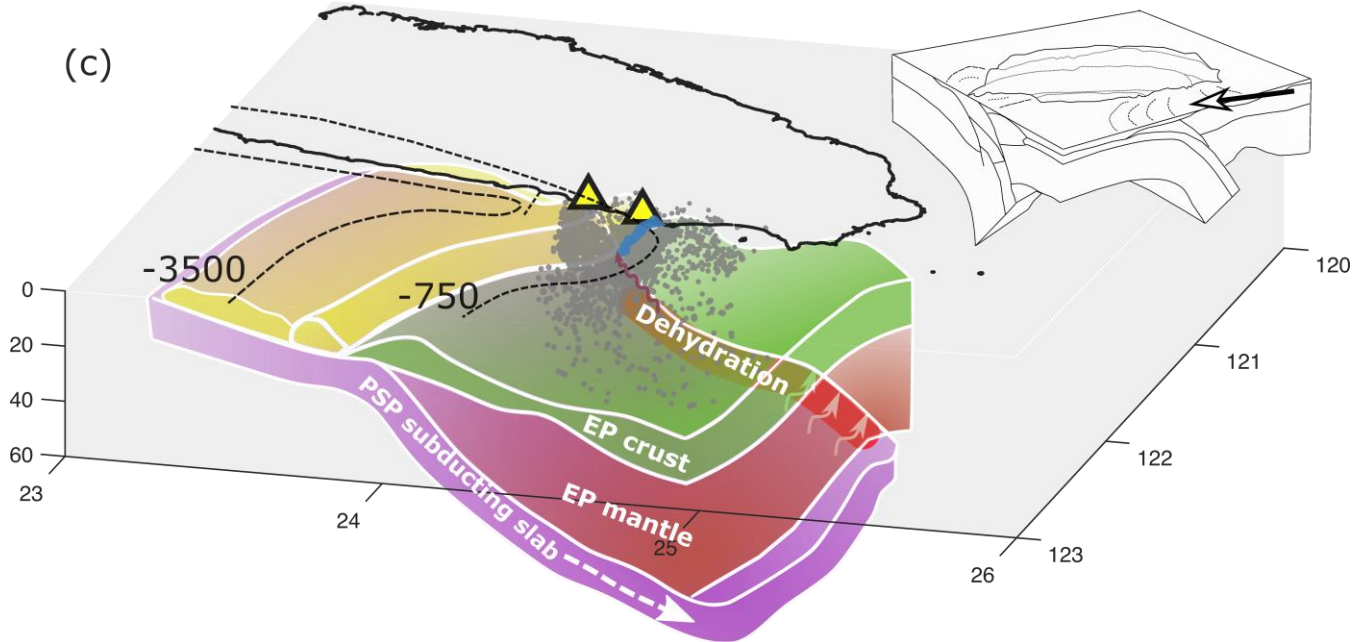
820

821 **Figure 6.** The spatial variation of locally maximum (a) shear strain (cross), dilation (open
 822 circle), and horizontal dilation (light open circle), and (b) rotations in the EW direction
 823 (triangle), the NS direction (diamond), and the vertical direction (square) during tremors
 824 1, 3, 7, and 9. The area of the pattern is scaled with the maximum value and denoted on
 825 the location of the mass center of the subarray. The triangles show the locations of Nanao

826 array stations NA01, 04, 05, 06, 07. The red star indicates the projected location of
827 tremor 7 obtained by the array processing method. The mass center of stations NA01, 04,
828 05, and 06 (red target) was taken as a reference point. The locations of the mass centers
829 (centroids) from different station configurations were concentrated in three regions.
830 Taking the subarrays giving maximum shear strain during tremor 3 in each region as
831 representative subarrays, we obtained (c) the temporal variation of shear strains, dilations,
832 and rotations during the tremors. The station configurations and the horizontal distances
833 between the mass centers of the subarrays and the reference point are labeled in the
834 legend. The temporal variation of shear strains, dilations, and rotations are shown in blue,
835 orange, and grey according to the distance from the reference point, from close to distant.
836



837



839

840 **Figure 7.** (a) The post-seismicity occurred after the Tohoku earthquake around the array
 841 over six months and the FK analysis of tremors 1, 3, 7, and 9. The yellow triangles
 842 represent the locations of the array stations. The southernmost one is station NAO05. The
 843 blue arrows indicate the back azimuths of tremor 1, 3, 7, and 9 according to the FK
 844 results. The projected location of tremor 7 (red cross) is determined by FK analysis using
 845 different subarrays. The red star is the largest event that occurred during these 6 months.
 846 From the profile of the seismicity distribution, a northeast dip slab (grey dash line) and a
 847 seismic gap (blue dash line) can be recognized at shallow depth. (b) Geographical
 848 distribution of higher V_p/V_s values ranging from 21 km (light gray) to 125 km (dark gray),
 849 modified from Lin et al. (2004). Dashed lines are isobaths of the Wadati-Benioff zone
 850 [Font et al., 1999]. The areas of high V_p/V_s anomalies are located above the western edge
 851 of the Ryukyu slab and the stations of Nanao array (yellow triangles) and NANB station
 852 (blue triangle) are located above the south end of high V_p/V_s anomalies. The square
 853 shows the region of (a). (c) Schematic of the tectonic setting for tremor triggering. The

854 heat flow (red line) originated from dehydration of the subducting oceanic slab or mantle
855 flow processes around the edge of the slab may provide additional fluid and heat to
856 shallow part when it propagated upward. The pore pressure may be elevated rapidly by
857 the penetrating fluid, heat, and high strain caused by the teleseismic wave. High pore
858 pressure may result in fractures (blue path) and activate rapid fluid flow under extreme
859 conditions, that is, of high volume of fluid, high temperature, and high strain. The grey
860 dots show the 6-month seismicity distribution, and the dashed lines are isobath lines
861 along the high elevation of accretion wedge and crust. The inset is the Taiwan tectonic
862 setting modified from Angelier (1986), where the arrow shows the view angle of our
863 schematic diagram.

864